Coupled Active Contours for Clue Cell Segmentation from Fluorescence Microscopy Images

Yongjian Yu[1] and Jue Wang[2]
[1]Axon Connected, LLC, Earlysville, VA 22936, U.S.A.
[2]Department of Mathematics, Union College, Schenectady, NY 12308, U.S.A.

Keywords: Segmentation, Active Contour, Level Set, Fluorescent Microscopy, Clue Cells.

Abstract: Bacterial vaginosis (BV) increases the risk for preterm birth. Immunofluorescent assay provides accurate counting of the clue cells. However, the massive data make it challenging to manually interpret. Towards automatic BV diagnostics, we present a coupled active contour method for segmenting the clue cells using dual-resolution, dual-channel microscopy. The method is formulated in the level set and parametric frameworks. A fast search locates potential clue cells in the low-resolution scan. Each cell is then imaged at high-resolution. The clue cells are segmented and quantified. The efficacy of the method is demonstrated using clinical data. Our method effectively delineates the boundaries of the cell and its nucleus simultaneously. It is efficient and practical. The clue cell detection results indicate a high accuracy for BV diagnosis.

1 INTRODUCTION

Preterm birth is the leading cause of neonatal mortality and morbidity. Approximately 10% of all births are preterm. The 2019 United Nations International Children's Emergency Fund (UNICEF) data reported an average rate of 18 deaths per 1,000 live births in 2018 (UNICEF 2019a). Globally, 2.5 million children died in the first month of life in 2018 – approximately 7,000 neonatal deaths every day. The latest report predicts that 52 million children under 5 will die between 2019 and 2030 (UNICEF 2019b), 47% of which happen during the first month. Preterm birth can lead to long-term medical care requirements and lifelong developmental disabilities. Just within the United States, preterm birth results in health care costs of over $26 billion annually. The financial and emotional toll to afflicted families is staggering. It is estimated that up to 50% of all preterm births are the result of vaginal biome abnormalities (Witkin 2015), such as bacterial vaginosis (BV), trichomoniasis, and yeast infections.

Through BV assays using wet mount microscopy, a physician manually selects and examines approximately 200 epithelial cells over the brightfield microscope slide, in order to evaluate the percentage of the clue cells, which are epithelial cells covered with bacteria. The process is subjective, time-consuming, and prone to error due to debris interference. The sensitive and accurate immunofluorescence (IF) assay improves the brightfield microscopic diagnosis of BV. Spectral features of the clue cells and debris augment the discrimination. Multi-resolution enables fast cell locating, closer examination of cell morphology and bacterial contamination. However, the advanced instrument generates massive data, making it a challenge for clinicians to find and identify the clue cells manually, in particular for point-of-care testing. It is highly valuable to develop an automated system for clue cell analysis to quickly and accurately assess BV.

A clinical sample is shown in Figure 1 at 4X and 40X objectives, respectively. The algorithm needs to first find epithelial cells using a 4X objective, and then separates them into clue cells and normal cells using a 40X objective. The problem of clue cell segmentation refers to the process of automatically identifying the cells for characterization and enumeration. In general, it is desirable to simultaneously detect the bacteria, nuclei, and cells of high scale range present in an image and the associate bacteria and nucleus with each cell.

Yu, Y. and Wang, J.
Coupled Active Contours for Clue Cell Segmentation from Fluorescence Microscopy Images.
DOI: 10.5220/0010265301440151
In *Proceedings of the 14th International Joint Conference on Biomedical Engineering Systems and Technologies (BIOSTEC 2021) - Volume 2: BIOIMAGING*, pages 144-151
ISBN: 978-989-758-490-9
Copyright © 2021 by SCITEPRESS – Science and Technology Publications, Lda. All rights reserved

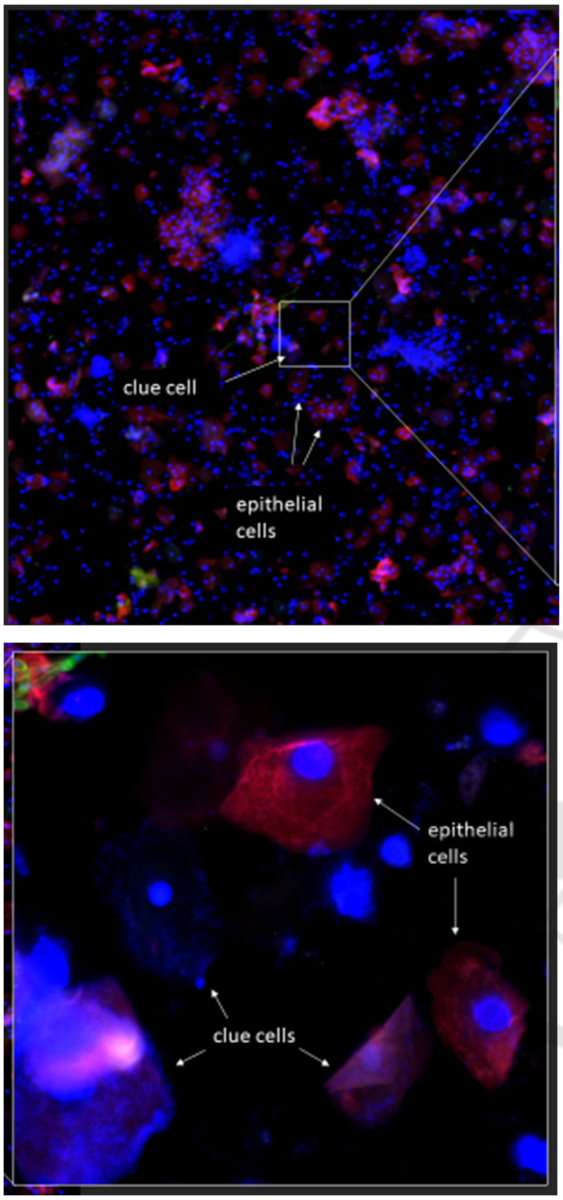

Figure 1: Distinguishing clue cells from normal epithelial cells. Top image: 4X objective. Bottom zoomed-in image: 40X objective showing clue cells (covered with small blue dots) and normal cells (little to no blue dots).

In the region-based variational minimization model, a level set function representation is introduced together with a contour length or curvature regularization (Chan and Vese 2001). The objects are segmented through similarity measures within the regions. This model is reformulated using a characteristic function representation with a length-equivalent total variation regularization (Zeune *et. al.* 2017). To achieve multiscale region-based segmentation, the regularization weight parameter decreases inversely proportionally to the steps through a Bregman iteration process. Finally a spectral analysis is applied to find the cells of interest.

Watershed transform segmentation has been used for segmenting partially overlapping objects. The watershed method is analogue to a landscape flooded by water. The watersheds are dividing contours upon which water from different basins meets, filling catchments corresponding to the local minima. The method is applied to segment epithelial cells from bright field microscopy (Tareef *et. al.* 2018).

We propose two coupled active contour (CAC) models. The main goal of this work is to present a multiscale segmentation method combining edge-region-based active contour methods at high-resolution with low-resolution watershed segmentation.

In our work, the vaginal samples are pre-stained using a pan cytokeratin (CK) cocktail and 46-diamidino-2-phenylindole (DAPI), the former labelling the entire cell and the latter for the nucleus only. The live epithelial cell is our target, thus it must have a nucleus. An advanced microscope acquires images at 385-nm and 490-nm channels using a 4X objective and a 40X objective. The area of the sample on the slide is about 15 mm by 15 mm, requiring 25 4X partially overlapped images to scan. The same area would need 2500 40X images (each of 2K by 2K pixels, 16-bit/pixel) to cover, which is prohibitive in time consuming and storage demanding. Therefore, a 4X fast search over the whole area followed by a 40X spotlight imaging balances the cell detection, characterization and engineering challenges.

Towards a fast, wide-range searching of epithelial cells, we process the 4X data by applying adaptive thresholding techniques to the CK-sensitive, 385-nm band to find the whole cells (CK blobs for short), and to the 490-nm channel for masking the nuclear blobs. Any clump of nuclei is identified by a size threshold and split using a marker-controlled watershed method. The nuclear markers are located as the local extended fluorescence maxima. A clump of cells is identified by the number of nuclei inside and spilt via the same watershed controlled by the nuclear markers. A 4X segmentation of the epithelial cells and associated nuclei is shown in Figure 2. The epithelial cells are in red color and the nuclei are blue inside the red. The isolated darker blue blobs are the white blood cells.

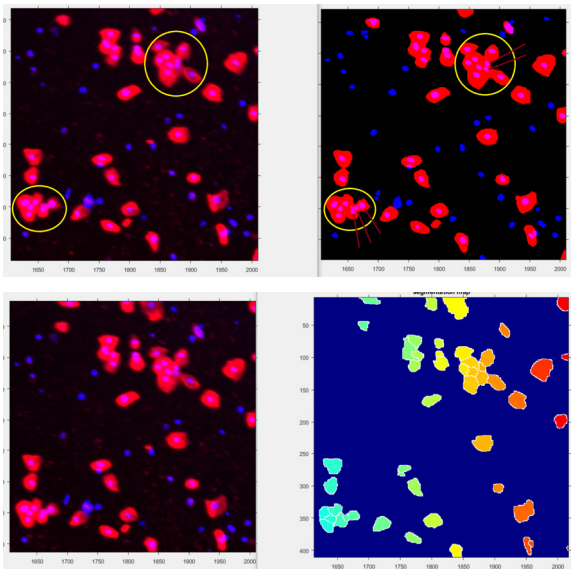

Figure 2: 4X composite image and segmentation of the epithelial cells and nuclei. The nuclei are the blue blobs inside the epithelial cells in red.

2 COUPLED ACTIVE CONTOUR MODELS

2.1 40X Segmentation of Isolated Epithelial Cell

We describe the first coupled active contour model for processing the 40X image to delineate the boundaries of the nucleus and membrane of an epithelial cell randomly selected from a pool of 4X segmentation. The goal is to identify whether the epithelial cell is a clue cell through detection and enumeration of bad bacteria in the cytoplasm region.

Let $\boldsymbol{I} = [I_n\ I_c]^T$ be a dual-band IF image (acquired with 40X objective) defined on the domain Ω, where the superscript T denotes transpose, and the subscripts indicate the nucleus or cell. Denote $\vec{\boldsymbol{C}}_n$ and $\vec{\boldsymbol{C}}_c$ a couple of nested closed curves. Let $\vec{\boldsymbol{C}}_c$ represent the zero-level set of a signed distance function $\phi: \Omega \to R$, such that $\vec{\boldsymbol{C}}_c = \{\boldsymbol{x}|\phi = 0\}$, with the interior being negative valued. The exterior of $\vec{\boldsymbol{C}}_c$ is specified by the regularized Heaviside function (Chan and Vese 2001),

$$\mathcal{H}_\epsilon(\phi) = \frac{1}{2}\left(1 + \frac{2}{\pi}\arctan\left(\frac{\phi}{\epsilon}\right)\right), \qquad (1)$$

where $\epsilon > 0$ is a small regularization parameter. The interior of $\vec{\boldsymbol{C}}_n$ is then defined as $\mathcal{H}_\epsilon(-\phi)$.

Likewise, let $\vec{\boldsymbol{C}}_n$ represent the zero-level set of a signed distance function $\varphi: \Omega \to R$, such that $\vec{\boldsymbol{C}}_n = \{\boldsymbol{x}|\varphi = 0\}$, with the exterior being negative valued. Similarly, we specify the interior of $\vec{\boldsymbol{C}}_n$ by $\mathcal{H}_\epsilon(-\varphi)$ and the exterior of C_n as $\mathcal{H}_\epsilon(\varphi)$. Therefore, the cytoplasm region is given by $\mathcal{H}_\epsilon(-\phi\varphi)$. The epithelial cell in dual band IF and level set functions are illustrated in Figure 3.

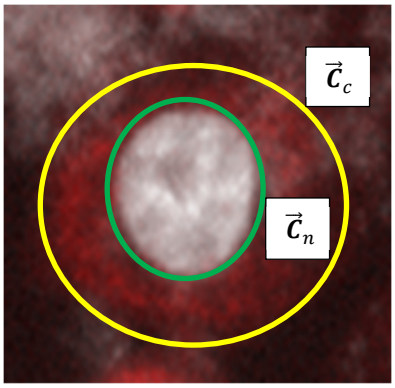

(a)

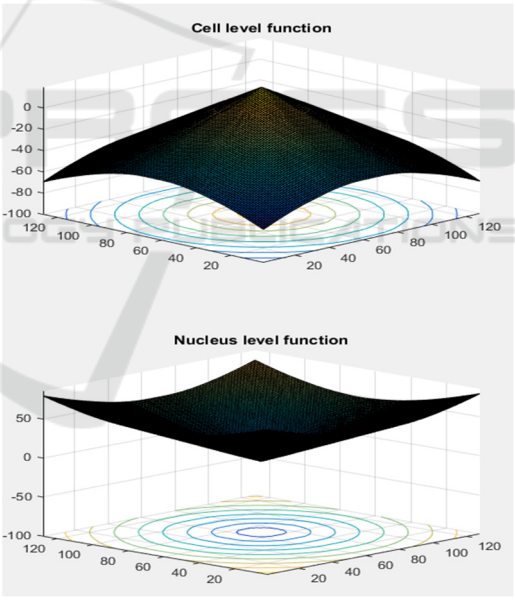

(b)

Figure 3: (a) Epithelial cell in dual band IF composite pseudo-colored image. The green and yellow contours depict boundaries of the nucleus and membrane, respectively. The central white region is the Dapi stained nucleus. The red region between contours is CK-labeled cytoplasm. (b) Level set functions of the nucleus and membrane boundaries.

We construct coupled flows on the vectorized level set $[\varphi\ \phi]^T$ that continuously attract $\vec{\boldsymbol{C}}_n$ toward the nuclear boundary while simultaneously attracting

$\vec{\boldsymbol{C}}_c$ toward the cell membrane boundary under the constraint that the former is completely enclosed by the latter. We devise the energy functional

$$E_0(\varphi,\phi) = \int_\Omega [\mathcal{H}_\epsilon(-\varphi)\,(I_n(\boldsymbol{x}) - u_n)^2 + \mathcal{H}_\epsilon(-\phi\varphi)(I_n(\boldsymbol{x}) - v_n)^2 + \mathcal{H}_\epsilon(-\phi\varphi)(I_c(\boldsymbol{x}) - u_c)^2 + \mathcal{H}_\epsilon(\phi)(I_c(\boldsymbol{x}) - v_c)^2]da \quad (2)$$

where $\boldsymbol{x} = (x, y), da = dxdy$, u_n and v_n represent the average I_n values of nucleus and cytoplasm, respectively; u_c and v_c represent the average I_c values of cytoplasm and the background (cell exterior region), respectively.

To keep both the interior and exterior curves smooth, we add length regularizations,

$$E_1(\varphi,\phi) = E_0(\varphi,\phi) + \int_\Omega [\lambda_1\delta_\epsilon(\varphi)|\nabla\varphi| + \lambda_2\delta_\epsilon(\phi)|\nabla\phi|]da \quad (3)$$

where $\delta_\epsilon(z) = \mathcal{H}_\epsilon'(z)$; λ_1 and λ_2 are positive weights for the nucleus and cell contours, respectively. A smaller weight corresponds to smaller objects. The goal is to find constrained minimizers to (3)

$$\min_{\substack{\varphi,\phi \\ \mathcal{H}_\epsilon(-\varphi)\subseteq\mathcal{H}_\epsilon(-\phi)}} E_1(\varphi,\phi) \quad (4)$$

where $\mathcal{H}_\epsilon(-\varphi) \subseteq \mathcal{H}_\epsilon(-\phi)$ is the cell-nucleus enclosure constraint that keeps the computed nuclear contour from migrating outside the membrane.

If any part of $\vec{\boldsymbol{C}}_n$ migrates outside $\vec{\boldsymbol{C}}_c$ during evolution, then the extruding area of that part is

$$B(\varphi,\phi) = \int_\Omega \mathcal{H}_\epsilon(\phi)\mathcal{H}_\epsilon(-\varphi)d\boldsymbol{x}. \quad (5)$$

The enclosure constraint dictates that $B(\varphi,\phi) = 0$ if the optimal segmentations of the membrane and nucleus boundaries are obtained. Relaxing the cell-nucleus enclosure constraint in (4), we approximate (4) by a non-constrained optimization with enclosure regularization

$$\min_{\varphi,\phi} E_1(\varphi,\phi) + \gamma B(\varphi,\phi). \quad (6)$$

Keeping the channels' regional statistics $\{u_n, v_n, u_c, v_c\}$ fixed, we derive the associated Euler-Lagrange equations for φ and ϕ, respectively, and formulate the coupled evolution equations following the idea of steepest descent,

$$\frac{\partial\varphi}{\partial t} = \delta_\epsilon(\varphi)[(I_n(\boldsymbol{x}) - u_n)^2 + \frac{\phi\delta_\epsilon(-\phi\varphi)}{\delta_\epsilon(\varphi)}((I_n(\boldsymbol{x}) - v_n)^2 + (I_c(\boldsymbol{x}) - u_c)^2) + \gamma\mathcal{H}_\epsilon(\phi) + \lambda_1\,\mathrm{div}\left(\frac{\nabla\varphi}{|\nabla\varphi|}\right)\Big] \quad (7)$$

$$\frac{\partial\phi}{\partial t} = \delta_\epsilon(\phi)[-(I_c(\boldsymbol{x}) - v_c)^2 + \frac{\varphi\delta_\epsilon(-\phi\varphi)}{\delta_\epsilon(\phi)}((I_n(\boldsymbol{x}) - v_n)^2 + (I_c(\boldsymbol{x}) - u_c)^2) - \gamma\mathcal{H}_\epsilon(-\varphi) + \lambda_2\,\mathrm{div}\left(\frac{\nabla\phi}{|\nabla\phi|}\right)\Big] \quad (8)$$

The equations are solved under Neumann boundary conditions.

2.2 Segmentation of Cells in Clutter

Clinical scans contain numerous cell clumps where multiple cells touch or overlap. The CAC level-set model will degrade if the epithelial cell picked for close examination is contacted with or inside a clump of cells. A second CAC parametric model is proposed towards algorithmic efficiency and higher numerical stability.

Define a pair of nuclear and cell segmenting curves, $\{\rho(\theta), \xi(\theta), \theta \in [0, 2\pi]\}$, that tend to move towards their corresponding boundaries simultaneously to minimize the following energy functional

$$E(\{\rho,\xi\}) = \int_0^{2\pi} \Big\{\frac{\alpha_1}{2}[\rho'(\theta)]^2 + \frac{\beta_1}{2}[\rho''(\theta)]^2 + \frac{\alpha_2}{2}[\xi'(\theta)]^2 + \frac{\beta_2}{2}[\xi''(\theta)]^2 + \mathcal{E}_1(\boldsymbol{R}_c + \rho(\theta)\hat{e}_r) + \mathcal{E}_2(\boldsymbol{R}_c + \xi(\theta)\hat{e}_r) + \mathcal{E}_3(\boldsymbol{R}_c, \rho(\theta), \xi(\theta))\Big\}d\theta \quad (9)$$

Subject to an enclosure constraint: $\rho(\theta) \le \xi(\theta)$,

where α_i and β_i are parameters that weigh elasticity and rigidity on the curves; $\hat{e}_r = \hat{e}_x\cos\theta + \hat{e}_y\sin\theta$, with $\hat{e}_x$ and $\hat{e}_y$ being unit vectors in the x and y direction, respectively. $\boldsymbol{R}_c = (x_c, y_c)$ is the position vector of the origin of the cell polar coordinate (r, θ), illustrated in Figure 4. It coincides with the centroid of the zoomed-in, pre-computed 4X nucleus mask of the same cell.

SCITEPRESS SCIENCE AND TECHNOLOGY PUBLICATIONS

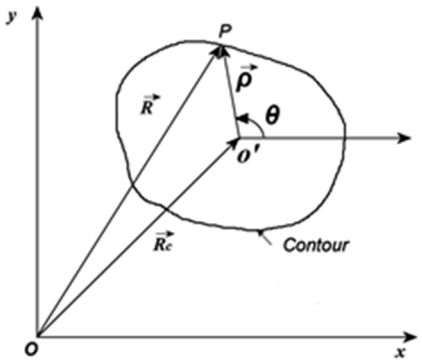

Figure 4: Polar coordinate system representation for segmenting cells in the clutter environment.

The $\mathcal{E}_i$'s are external energy derived from the image $\boldsymbol{I} = [I_n\, I_c]^T$ and *a priori* 4X segmentation such that they take small values near the boundaries of associated nucleus and cell. $\mathcal{E}_1$ and $\mathcal{E}_2$ are driven by the localized edges in I_n and I_c,

$$\mathcal{E}_1(x,y) = -\|\nabla I_n(x,y)\|^2, \tag{10}$$

$$\mathcal{E}_2(x,y) = -\|\nabla I_c(x,y)\|^2. \tag{11}$$

The $\mathcal{E}_3$ is region-based. The directional energy along each radial direction is defined as

$$\begin{aligned}\mathcal{E}_3(\theta|\boldsymbol{R}_c,\rho,\xi) = &\int_0^{\rho}(I_n(r)-u_n)^2\,dr \\ &+\int_{\rho}^{\xi}[(I_n(r)-v_n)^2 \\ &+(I_c(r)-u_c)^2]dr \\ &+\int_{\xi}^{\infty}(I_c(r)-v_c(\theta))^2\,dr\end{aligned} \tag{12}$$

where $I_n(r)$ denotes the profile of $I_n(x,y)$ along the polar axis r at point $\boldsymbol{R}_c$ with angle θ; $v_c(\theta)$ denotes the representative I_c value of the clutter or background as a function of θ. The u_n, v_n and u_c omni-directional statistics are computed as the median values using the zoomed-up, registered 4X mask of the cell. In each direction, v_c is computed as the median value of I_c in the neighboring cell or in the background. Figure 5 illustrates how these statistics are measured with the aid of a 4X mask and neighborhood adjacency relation. We fix these values during the contour evolution. The segmentation is the zoomed-up 4X mask registered with the 40X image. It is the angle sensitivity that empowers segmenting cells in a clump environment.

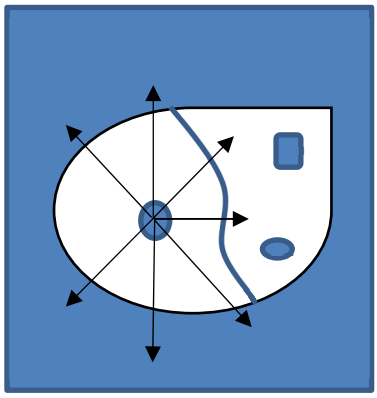

Figure 5: Estimation of the omni-directional statistics $\{u_n, v_n, u_c\}$ for the nucleus and cell and directional background statistics v_c. The cell with outward arrows is the cell under examination. Other touching cells are the clutters.

We first lift the enclosure constraint in (9) and derive the Euler-Lagrange equations for the optimal coupled active contours. The contour evolution equations are then formulated as follows,

$$\frac{\partial\rho}{\partial t} = \alpha_1\rho''(\theta) - \beta_1\rho^{(4)}(\theta) + F_1 + f_1, \tag{13}$$

$$\frac{\partial\xi}{\partial t} = \alpha_1\xi''(\theta) - \beta_1\xi^{(4)}(\theta) + F_2 + f_2, \tag{14}$$

where $-F_1 = \frac{\partial\mathcal{E}_1}{\partial\rho} = \frac{\partial\mathcal{E}_1}{\partial x}\cos\theta + \frac{\partial\mathcal{E}_1}{\partial y}\sin\theta,$

$-F_2 = \frac{\partial\mathcal{E}_2}{\partial\xi} = \frac{\partial\mathcal{E}_2}{\partial x}\cos\theta + \frac{\partial\mathcal{E}_2}{\partial y}\sin\theta,$

which are evaluated on evolving contours ρ and ξ, respectively. Using the level set functions φ and ϕ for region representations, we derive the regional forces as

$$\begin{aligned}f_1 = &(I_n(\rho)-u_n)^2 + \frac{\phi\delta_\epsilon(-\phi\varphi)}{\delta_\epsilon(\varphi)}((I_n(\rho)- \\ &v_n)^2 + (I_c(\rho)-u_c)^2) + \gamma\mathcal{H}_\epsilon(\phi),\end{aligned}$$

$$\begin{aligned}f_2 = &-\big(I_c(\xi)-v_c(\theta)\big)^2 + \frac{\varphi\delta_\epsilon(-\phi\varphi)}{\delta_\epsilon(\phi)}((I_n(\xi)- \\ &v_n)^2 + (I_c(\xi)-u_c)^2) - \gamma\mathcal{H}_\epsilon(-\varphi),\end{aligned}$$

where the last terms serve as enclosure regularization forces to ensure nucleus-cell enclosure similar to (7) and (8).

The first two terms in (13) and (14) comprise the axially directed internal forces; the last two terms represent the external forces in the axial direction driven by local edges and regional statistics. The internal and external forces compete with each other; the former resists bending while the latter guides the contour towards the image edges. The contour of the 40X image is initialized as the boundary of the

corresponding 4X watershed segmentation, and then 10-fold rescaled and post-processed morphologically. The morphological processing rectifies the cell shape and size to ensure the separation of adjacent cells.

2.3 Identification and Characterization of Clue Cells

Once the epithelial cells are segmented, the clue cells are identified via bacterial detection over the epithelial cytoplasm. In order to detect the tiny bacteria in the noise, we apply a detail-preserving, non-local mean filter to suppress the noise. The bacteria are then found by adaptive thresholding to the cleaned image, illustrated in Figure 6.

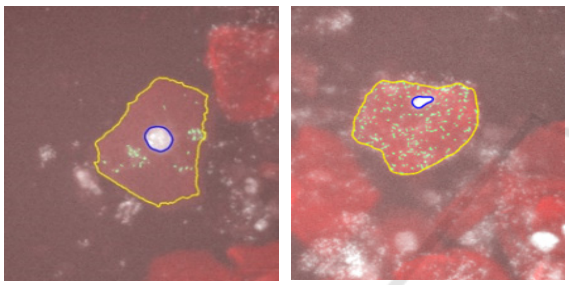

Figure 6: Bacterial detection on epithelial cytoplasm.

We quantify the bacterial contamination of an epithelial cell using a single metric R, the ratio between the bacterial area and cytoplasm area. The likelihood of the clue cell is calculated using the following expression:

$$P = \Phi\left(\frac{R-\mu}{\sigma}\right)$$

where $\Phi(x)$ is a strictly increasing and continuous function. In this work, Φ takes the form of a cumulative normal Gaussian distribution function; the μ and σ are parameters defining the border between normal and clue cells. They are determined under user supervision using a labeled training dataset.

3 NUMERICAL IMPLEMENTATION

We devise numerical algorithms for solving the coupled evolution equations (7) and (8) iteratively. The level set function φ and ϕ are initialized through the following steps. We first resize the 4X image and mask of an epithelial cell of choice to 40X, and then register the zoomed-up 4X image with the acquired 40X image via cross-correlation. The registered, zoomed-up 4X mask is used as the level set initialization. The statistics $\{u_n, v_n, u_c, v_c\}$ are updated during each iteration. Towards computational efficiency, values of φ and ϕ are updated in their respective narrow bands around their zero level sets. Re-initialization is applied using a fast marching scheme (Fatemi and Sussman 1995). The iteration stops when any watershed line is crossed by any cell contour. To achieve numerical stability, image forces are normalized for each step such that the combined image forces only update the contour by one pixel.

The contour evolution equation (13) is discretized as follows,

$$\frac{\rho_i^{n+1}-\rho_i^n}{\Delta t} = \frac{\alpha_1}{h^2}\left[\rho_{i\oplus 1}^n - 2\rho_i^n + \rho_{i\ominus 1}^n\right] - \frac{\beta_1}{h^4}\left[\left(\rho_{i\oplus 2}^n - 2\rho_{i\oplus 1}^n + \rho_i^n\right) - 2\left(\rho_{i\oplus 1}^n - 2\rho_i^n - \rho_{i\ominus 1}^n\right) + \left(\rho_i^n - 2\rho_{i\ominus 1}^n + \rho_{i\ominus 2}^n\right)\right] + F_{1,i}^n + f_{1,i}^n,$$

where Δt is the time step and h is the angle increment, $h = \frac{2\pi}{N}$, N is the number of angles, $\theta_i = ih$, $\rho_i^n = \rho(\theta_i, n\Delta t)$, $\oplus$ and $\ominus$ are modulo N addition and subtraction, respectively.

$$f_{1,i}^n = f_1(\rho_i^n, \phi^n, \varphi^n),$$

and

$$F_{1,i}^n = -\left(\cos\theta_i \frac{\partial \varepsilon_1}{\partial x} + \sin\theta_i \frac{\partial \varepsilon_1}{\partial y}\right)\Big|_{x_c+\rho_i^n\cos\theta_i,\, y_c+\rho_i^n\sin\theta_i}.$$

The contour evolution (14) is discretized similarly. We take N to be 64 in our tests. The set of linear equations is put into a matrix form and solved using an implicit scheme where Δt is set to unity.

4 EXPERIMENTS AND RESULTS

We evaluate the performance of proposed CAC parametric and CAC level models using a sample of seven cells. Three cells are isolated intact cells and the other four belong to two 2-cell clusters. Example segmentation results are shown in Figures 7 and 8, along with a comparison to the multi-pass watershed segmentation (Tareef *et. al.* 2018). The Dice similarity coefficient and Jaccard index are used for measuring the segmentation quality against the expert drawn ground truth. The Dice similarity coefficient is a spatial overlap index with values in the range [0,1]. A similarity of 1 means a perfect match in the segmentation. The Jaccard index calculates the size of intersection of

two binary images divided by the size of their union. This index compares members of two sets for which are shared and which are distinct. It is in the range from 0% to 100%, the higher the percentage, the more similar the two sets. The metrics are listed in Tables 1 and 2.

To further demonstrate and assess the performance of our algorithm, we analyze an example patient sample for BV diagnosis based on the 20% clue cell diagnostic rule, and compare the results with clinician detection. From the patient sample an ensemble of 200 entries were randomly selected. 48 of 55 clue cells (positive) and 134 of 145 normal epithelial cells (negative) identified by CAC match the clinician detection. The sensitivity = 0.81, specificity = 0.95, precision = 0.87, and accuracy = 0.91. The confusion matrix is illustrated in Table 3. Both the clinician and CAC detection agree that the patient is BV positive. Our method segments the cell boundaries very accurately for 80% of the cells. Bacteria clumps and bordering clue cells result in the false positives. In the case where the cell images are out of focus, CAC correctly identifies the cells as non-clue (negative).

The algorithm is implemented in C++ and integrated with a proprietary digital fluorescence microscope operated with Intel i9, 8-core processor and 32 GB RAM in the Windows 10 Pro environment. The BV scan analysis software processes a patient sample mounted on a slide. The imaging pipeline begins after a sample slide is loaded onto the motorized stage of the microscope. The system first acquires 25 4X-objective sub-scan images covering the region of the slide, and meanwhile searches, in parallel, for all epithelial cells with the 4X search algorithm, resulting in up to 200 cells randomly distributed for further detailed analysis. Then, after switching to a 40X objective and stage movement, it refocuses at each of the selected 4X cell's positions, images at 40X of each cell, and applies the 40X segmentation algorithm to contour the cell boundary, followed by bacteria detection, quantification, and clue cell ranking. The total time of the entire imaging pipeline running in the microscopic operating system takes less than 10 minutes. The BV processing time is less than half of that total time. The time for LED exposure, 40X objective point-wise refocusing, stage movement, and data transferring from the digital camera to computer is all included in the 10 minutes.

Our detection algorithm is efficient and practical. It performs well and demonstrates a high accuracy in the test-heavy samples.

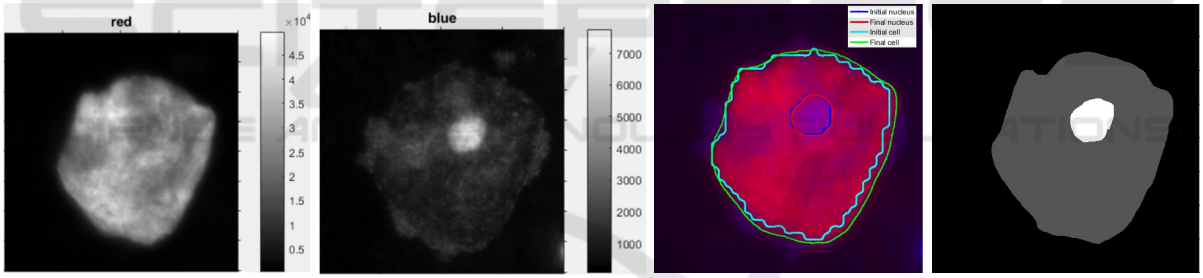

(a) (b) (c) (d)

Figure 7: Segmentation of an isolated epithelial cell. (a) CK channel I_c. (b) DAPI channel I_n. (c) CAC level set segmentation. The nucleus and membrane contours are in red and green, with initialization in blue and cyan, respectively. (d) Ground truth: nucleus (bright) and cytoplasm (gray).

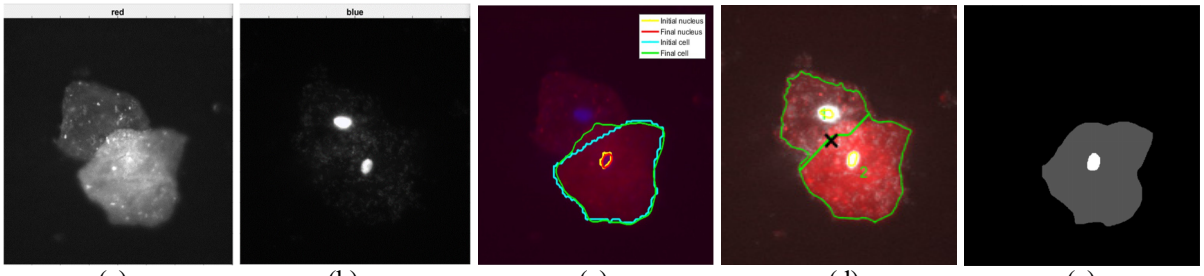

(a) (b) (c) (d) (e)

Figure 8: Segmentation of partially overlapping epithelial cells. (a) CK channel I_c. (b) DAPI channel I_n. (c) CAC parametric segmentation for the bottom cell. (d) Multi-pass watershed. (e) Ground truth: nucleus (bright) and cytoplasm (gray).

Table 1: Average Dice Index for Nucleus and Cell.

	Single cell		Overlapped	
	Nucleus	**Cell**	**Nucleus**	**Cell**
CAC level set	0.86	0.98	0.87	0.95
CAC parametric	0.84	0.98	0.82	0.97
Multi-pass watershed	0.81	0.98	0.87	0.95

Table 2: Average Jaccard Index for Nucleus and Cell.

	Single cell		Overlapped	
	Nucleus	**Cell**	**Nucleus**	**Cell**
CAC level set	0.74	0.96	0.76	0.89
CAC parametric	0.68	0.96	0.68	0.94
Multi-pass watershed	0.65	0.95	0.74	0.89

Table 3: Confusion Matrix for CAC Method.

Total = 200		**Actual**	
		Positive	Negative
Predicted	Positive	True Positive TP = 48	False Positive FP = 7
	Negative	False Negative FN = 11	True Negative TN = 134

5 CONCLUSIONS

We have developed two coupled active contour (CAC) models, one with a level set formulation and the other parametrically, for segmenting the clue cells and nuclei from the dual-band fluorescence microscope scans of vaginal samples for bacterial vaginosis diagnosis. Our models cannot be categorized simply as a vectorized active contour method because the channels are treated independently and the curves evolve cooperatively. The model is augmented with a coarse-resolution preprocessing. The imposed enclosure constraint is tailored to the nested annular shapes. The CAC method is adaptive for the complex cluttered cell environment, where the polar model is devised as coupled parametric snakes that are driven by local edge forces and long-range regional forces formulated in the level set representation. While application-oriented, our effort adds new contributions to the active contour methodology.

REFERENCES

R. E. Behrman, A.S. Butler (editors), Preterm birth: causes, consequences, and prevention, Washington, DC: The National Academies Press, 2007.

T. Brox and J. Weickert, "Level set segmentation with multiple regions", *IEEE Trans. Image Process.*, vol. 15, no. 10, pp. 3213-3218, 2006.

T. F. Chan and A. Vese, "Active contours without edges", *IEEE Trans. Image Process.*, vol. 10, no. 2, pp. 266-277, 2001.

E. Fatemi and M. Susman, "An efficient interface preserving level-set re-distancing algorithm and its application to interfacial incompressible two-phase flow", *SIAM J. Sci. Statist Comput.*, vol. 158, no. 1, pp. 36-58, 1995.

A. Farr, H. Kiss, M. Hagmann, S. Machal, I. Holzer, V. Kueronya, P.W. Husslein and L. Petricevic, "Role of lactobacillus species in the intermediate vaginal flora in early pregnancy: a retrospective cohort study", *PLoS One*, vol. 10, no. 12, e0144181, 2015.

A. Tareef, Y. Song, H. Huang, D. Feng, M. Chen, Y. Wang and W. Cai, "Multi-pass fast watershed for accurate segmentation of overlapping cervical cells", *IEEE Trans. Med. Imag.*, vol.37, no.9, pp. 2044-2059, 2018.

UNICEF 2019a, The United Nations International Children's Emergency Fund, "Neonatal mortality", Sept. 2019. https://data.unicef.org/topic/child-survival /neonatal-mortality.

UNICEF 2019b, United Nations International Children's Emergency Fund, Levels and trends in child mortality, United Nations Inter-Agency Group for Child Mortality Estimation (UN IGME), Report 2019. https://data.unicef.org/resources/levels-and-trends-in-child-mortality.

S.S. Witkin, "The vaginal microbiome, vaginal anti-microbial defence mechanisms and the clinical challenge of reducing infection-related preterm birth", *BJOG*, vol. 122, no. 2, pp. 213-218, 2015.

L. L. Zeune, G. van Dalum, L.W.M.M. Terstappen, S.A. van Gils and C. Brune, "Multiscale segmentation via Bregman distances and nonlinear spectral analysis", *SIAM J. Imag. Sci.*, vol. 10, no. 1, pp. 111-146, 2017.